T. Sponfeldner, I. Boxx, F. Beyrau, Y. Hardalupas, W. Meier, A.M.K.P. Taylor

On the alignment of fluid-dynamic principal strain-rates with the 3D flamelet-normal in a premixed turbulent V-flame

On the alignment of fluid-dynamic principal strain-rates with the 3D flamelet-normal in a premixed turbulent V-flame

Authors: T. Sponfeldner[2], I. Boxx[1], F. Beyrau[2], Y. Hardalupas[2], W. Meier[1], A.M.K.P. Taylor[2]

Affiliations:

[1] Institut für Verbrennungstechnik, Deutsches Zentrum für Luft- und Raumfahrt (DLR), D-70569 Stuttgart, DE

[2] Department of Mechanical Engineering, Imperial College London, SW7 2AZ, London, UK

Corresponding author: Dr. Isaac Boxx. Isaac.boxx@dlr.de

Abstract

Statistics of the alignment of fluid-dynamic principal strain-rates and the local flamelet-normal in a premixed turbulent V-flame (methane-air, $Re_t = 450$, $\varphi = 0.8$) were measured experimentally using simultaneous stereoscopic particle image velocimetry (SPIV) and planar laser-induced fluorescence of OH (OH-PLIF). The use of a second OH-PLIF sheet, oriented in a crossed-plane imaging configuration enabled conditioning of the statistics with respect to through-plane flame orientation. The statistics show the geometric alignment changes significantly with the distance between the flame and the location where the strain-rate field is evaluated. It was observed that approximately 30η upstream of the flame, the fluid-dynamic principal strain-rates show no preferential alignment with the flamelet. With increasing proximity to the flame, the most extensive principal strain-rate is observed to align preferentially perpendicular to the local flamelet-normal. In the immediate vicinity of the flame, where local fluid-dynamics are dominated by dilatation, the principal extensive strain-rate is observed to align preferentially parallel to the local flamelet-normal. The realignment of the principal strain-rates in the immediate vicinity of the flame is clearly the result of local flow acceleration caused by heat-release at the reaction zone. As the most extensive principal strain-rate tends to align preferentially perpendicular to the local flamelet-normal outside the region of heat-

release, the data indicate that high scalar gradients observed ahead of the flamelet are produced by the local turbulent flow-field, rather than destroyed by it.

Keywords

Turbulence-flame alignment, turbulence-flame interaction, turbulent premixed flames, cinematographic crossed-plane planar laser induced fluorescence, cinematographic particle image velocimetry,

1 Introduction

Understanding the interaction of fluid-dynamic strain-rate and scalar dissipation is critical to the modeling of turbulent flames. Scalar dissipation rate of the reaction progress variable, c, is defined as $N_c = \kappa(\nabla c \cdot \nabla c)$, were κ is its diffusivity. Scalar dissipation rate is an important quantity in turbulent flame models and recently a transport equation was proposed which identified mechanisms affecting the scalar dissipation rate. It is given by [1, 2],

$$\rho \frac{DN_c}{Dt} = 2\rho N_c \frac{\partial u_i}{\partial x_i} - 2\rho\kappa \frac{\partial c}{\partial x_i} S_{ij} \frac{\partial c}{\partial x_j} + \frac{\partial}{\partial x_j}\left(\rho\kappa \frac{\partial N_c}{\partial x_j}\right)$$
$$- 2\rho\kappa^2\left[\frac{\partial}{\partial x_j}\left(\frac{\partial c}{\partial x_i}\right)\right] + 2\kappa \frac{\partial c}{\partial x_i} \frac{\partial \dot{\omega}}{\partial x_i},$$
(1)

where ρ is the fluid density, $\dot{\omega}$ is the reaction rate and $S_{ij} = 1/2\left(\partial u_i/\partial x_j + \partial u_j/\partial x_i\right)$ is the fluid-dynamic strain-rate tensor. The term on the left-hand side of Eq. (1) denotes the temporal and convective changes of the scalar dissipation rate. The first term on the right-hand side describes the effect of dilatation on the scalar dissipation rate, followed by the effect of turbulence-flame interaction. The third, fourth and fifth terms describe the changes of N_c due to diffusive fluxes, molecular dissipation and chemical reactions, respectively. This study focuses on the second term in Eq. (1), *i.e.* the effect of fluid-dynamic strain on the scalar dissipation rate.

One way to better understand how turbulence interacts with the flame is by studying the geometric alignment between the flame surface normal direction, $\vec{n} = -\nabla c / |\nabla c|$, and the direction of the principal strain-rates. The orientation is a key mechanism of turbulence-flame interaction and was derived from the interaction of passive scalar gradient fields with non-reacting flows [3]. The principal strain-rates are calculated from the strain-rate tensor, S_{ij}, by solving the eigenvalue equation and sorting the eigenvalues in descending order, $\gamma_1 > \gamma_2 > \gamma_3$. By convention, the largest eigenvalue, γ_1, is called the most extensive principal strain-rate and the smallest eigenvalue, γ_3, is called the most compressive principal strain-rate. The corresponding eigenvectors represent their direction. The orientation between the principal strain-rates and the flame surface normal direction determines whether scalar gradients are produced or destroyed by the turbulence. Scalar gradients are produced when the flame surface normal direction, $\vec{n}$, aligns preferentially perpendicular to the most <u>extensive</u> principal strain-rate, *i.e.* the most <u>compressive</u> principle strain-rate aligns preferentially parallel to the flame surface normal direction.

Studies have shown that in non-reacting turbulent flows, scalar dissipation occurs predominantly in thin, sheet-like structures throughout the flow [4, 5] that tend to align perpendicular to the most extensive principal strain-rate. This results from turbulence acting to reduce the separation of scalar isosurfaces in the flow and thereby generating gradients that drive dissipation. As the reaction zone of a turbulent flame is associated with a strong scalar gradient, passive scalar mixing physics are frequently used to model turbulent flame dynamics [6]. Recent studies, however, have raised questions as to the validity of this approach.

Chakraborty and Swaminathan [7, 8], applied direct numerical simulation (DNS) to investigate the role of the Damköhler number on strain-flame alignment characteristics in premixed turbulent flames and report the most extensive principal strain-rate to align preferentially parallel to the local flamelet-normal vector at the flamelet. This finding was confirmed experimentally by Hartung *et al.* [9], using simultaneous PIV/OH-PLIF measurements. From these results it was concluded that turbulence destroys scalar gradients in flames, raising questions as to the validity of

using passive scalar turbulence physics to model premixed turbulent flames. A later experimental study by Steinberg *et al.* [10] however, reports a clear tendency of the most extensive principal strain-rate to align preferentially perpendicular to the local flamelet-normal, suggesting that scalar gradients are indeed produced by turbulence rather than destroyed by it and therefore that passive scalar physics apply in modelling premixed turbulent flames. The apparent inconsistency between these two studies is a key motivation for the present work.

The aim of this study was to investigate and quantify the alignment of the most extensive principal strain-rate with respect to the local flamelet-normal in a premixed turbulent flame at atmospheric pressure conditions. This was accomplished through the simultaneous application of stereo-PIV (to measure the in-plane velocity and strain-rate field) and crossed-plane OH-PLIF (to identify the flamelet-normal direction, conditioned with respect to through-plane flame orientation). The measurements were used to statistically characterize the angle θ_1 between the local flamelet-normal direction and the most extensive principal strain-rate at distances ranging from 0.8mm to 3.6mm upstream of the flamelet. These data help to understand the competition between dilatation and fluid-dynamic strain and clarify the role of turbulent fluctuations in the production and / or destruction of scalar gradients ahead of the premixed turbulent flame.

2 Experiment and diagnostics

2.1 Burner

The burner used in this study is illustrated in Fig. 1. It consists of a 600mm long aluminium duct with square (62 × 62mm) cross-section. A fractal-grid turbulence generator plate (Hurst and Vassilicos [11]) was mounted 100mm upstream of the burner exit. Premixed reactants enter the burner through a 4-injector manifold at the base of the duct. The reactant stream (methane-air, $\varphi = 0.8$) is seeded with titanium-dioxide particles (1μm nominal diameter) to facilitate SPIV imaging. The reactant stream passes flow-conditioning elements consisting of a series of perforated

plates (1mm hole-diameter), bead-beds (3 layers, 10mm diameter glass beads) and a honeycomb flow-straightener (5mm cell size, 50mm length). The turbulent V-flames were stabilized on a 1.02mm diameter stainless-steel wire mounted 10mm downstream of the burner exit, *i.e.* 110mm downstream of the turbulence grid.

The turbulent flow-field generated in this burner was characterized under isothermal conditions using a single-component hot-wire anemometer. The relevant fluid-dynamic and flame parameters are listed in Table 1. The integral length scale, L, and the Taylor microscale, λ, were computed from the temporal autocorrelation of the axial (streamwise) velocity. Assuming homogeneous, isotropic turbulence, the Kolmogorov length scale, η, was estimated according to Eq. (2) [12],

$$\eta = \left(\frac{\nu^2 \lambda^2}{30 u'^2} \right)^{1/4}. \tag{2}$$

The Damköhler (Da) and Karlovitz (Ka) numbers were calculated using the definitions given in [13]. The values listed in Table 1 indicate the flame measured in this study lists in the corrugated flamelet regime [14]. The values listed in Table 1 are consistent with those determined from 2-component PIV measurements taken in the same burner[28].

2.2 Stereoscopic particle image velocimetry

Stereoscopic particle image velocimetry (SPIV) was applied in the plane parallel to the axial flow direction and perpendicular to the flame stabilizing wire. The SPIV system has been extensively described in the literature [15, 16], which is why only a brief description is given below.

The system consisted of a dual-cavity, diode-pumped solid-state (DPSS) Nd:YAG laser (Edgewave IS-6IIDE, ≈ 2.6mJ/pulse, 7.5ns and 20μs pulse energy, duration and separation, respectively) and a pair of CMOS cameras (LaVision, HSS6 and HSS8), shown in Fig. 2. The laser was formed into a collimated sheet of ≈ 20mm height via a cylindrical telescope and focused to a

0.6mm waist with a third cylindrical lens. The CMOS cameras were positioned on opposite sides of the SPIV sheet arranged in a forward-scatter imaging configuration. The Mie-scattered light was collected via 200mm focal length, f/11 objective lenses (Nikkor). Scheimpflug-adaptors were used to compensate for defocussing of the images caused by off-axis imaging. Image distortion due to off-axis orientation of the cameras was corrected using a dual-plane image target (LaVision, Type 7). The same target was also used for mapping the fields of view of the SPIV and PLIF systems to one another.

The SPIV system acquired 2048 dual-frame images per measurement run, for approximately 0.66s run duration. Twelve measurement runs were acquired in this study, resulting in over 24000 images and approximately 8s of total measurement time. Velocity vectors were extracted from the particle images using an adaptive multi-pass cross-correlation algorithm (LaVision 7.2) with interrogation windows ranging from 64×64 to 32×32 pixel, and 50% overlap, resulting in vector resolution and spacing of 0.8mm and 0.4mm, respectively. PIV vector validation and a 3×3 Gaussian smoothing filter was applied to the vector fields for the subsequent analysis.

2.3 Planar laser induced fluorescence

Planar laser-induced fluorescence imaging of the OH radical (OH-PLIF) was applied simultaneously in two imaging planes. The first imaging plane was coincident with that of the SPIV system. The second imaging plane intersected the first at an angle of $\psi = 48°$, as shown in Fig. 3. Data acquired in the first imaging plane was used to identify the reaction zone location of the flame in the SPIV measurement plane. The second OH imaging plane was used to determine the out-of-plane component of the 3D flamelet-normal vector at points along the line-of-intersection of the two planes. As will be discussed later, this information was used to condition the flame-strain alignment statistics against local flamelet orientation.

The first and second OH-PLIF systems used frequency-doubled dye lasers (Sirah Credo and Cobra-Stretch HRR, respectively), operated with Rhodamine-6G in ethanol and pumped by separate

frequency-doubled DPSS lasers (Edgewave IS-8IIE, with 4mJ and 5mJ pulse-energies, respectively). The first and second lasers produced 130 and 260μJ/pulse at 283.2nm, respectively. Both lasers were tuned to the $Q_1(7)$ line of the $A^2\Sigma^+$-$X^2\Pi$ (1,0) transition at 283.2nm using a laminar reference flame and a photo multiplier tube. Wavelength tuning was checked daily and monitored between imaging runs. The UV pulses were temporally interlaced between the first and second pulse of the SPIV system, offset from one-another by 2μs to avoid cross-talk. The first and second PLIF lasers were formed into collimated light sheets approximately 30mm tall using cylindrical telescope optics and then focused to sheets of $\approx$ 0.3mm and 0.6mm thickness, respectively, using cylindrical lenses. The first OH-PLIF sheet was overlapped with the SPIV sheet using a dichroic mirror as shown in Fig. 2. The second OH-PLIF sheet was formed by passing the laser through a set of cylindrical lenses rotated 48° and transmitted into the probe region from the opposite side of the burner using a second dichroic mirror. The second dichroic mirror prevented retro-reflection of the 532nm beam into the second PLIF laser system. To ensure accurate and reproducible alignment of the crossed OH-PLIF sheets in this experiment, a custom-made sheet-profiling instrument similar to [17] (consisting of a 1.3 megapixel CCD camera coupled with a 105mm, f/2.8 macro lens through an adjustable lens-tube assembly)was used to monitor the orientation of the two PLIF sheets during alignment before imaging runs. With this device the angle between the two sheets was measured to be 48° in the near- and far-field.

The OH-PLIF signal was recorded on CMOS cameras (LaVision, HSS5) equipped with external two-stage, lens-coupled intensifier (LaVision, HS-IRO). Fluorescence from the $A^2\Sigma^+$-$X^2\Pi$ (1,1) and (0,0) transitions of OH at around 308nm was collected with 100mm, f/2.0 objective lenses (Halle). Background flame luminosity and elastic scattering of the 283.2nm laser from particles in the flow were eliminated through intensifier gating and band-pass interference filters, respectively. Image de-warping and spatial calibration of the PLIF images was accomplished by imaging dual-plane calibration targets aligned to each laser-sheet and applying a pinhole camera model de-warping algorithm (LaVision Davis 7.2). The coordinate system of the first OH-PLIF measurement system

was mapped to that of the SPIV systems based on images of a calibration target carefully aligned with the laser sheet and imaged simultaneously by both systems.

3 Data reduction

The goal of these measurements was to statistically characterize the alignment of the most extensive principal strain-rate with respect to the local flamelet-normal direction as a function of the distance upstream from the flamelet. This required robust identification of both the local 3D flamelet-normal vector and the direction of the most extensive principal strain-rate in the planar measurement data. The data-processing steps used to accomplish this are outlined below.

3.1 Principal strain-rates

To compute the full, nine-component strain-rate tensor, $S_{ij} = 1/2 \left(\delta u_i / \delta x_j + \delta u_j / \delta x_i \right)$, three-dimensional velocity field data (*e.g.* from parallel-plane stereo-PIV measurements [18]) is required. The (planar) stereo-PIV measurements acquired in this study yield only four components of the strain-rate tensor. We note however that the in-plane principal strain-rates correspond to the 3D principal strain-rates in regions where the flow is locally two-dimensional and / or where the *z*-(through-plane) axis corresponds to one of the principal strain-rate axes [19]. Although various methodologies exist for conditioning velocity-field data to regions of the flow that are locally two-dimensional, *e.g.* by restricting the analysis to regions where the in-plane derivatives of the through-plane velocity, $\partial u_z / \partial x$ and $\partial u_z / \partial y$, are small compared to the 2-norm of the corresponding strain-rate component [10], such methodologies introduce uncertainties which are difficult to quantify and do not account for the through-plane component of the local flamelet-normal.

In the present study, the local through-plane orientation of the flamelet-normal was used as a conditioning parameter for the strain-rate data. It is well-established [9, 10, 20], that the orientation of the local flamelet-normal is strongly correlated with the directions of fluid-dynamic principal

strain-rates. As the principal strain-rates are orthogonal, it is reasonable to conclude that flamelets which are locally orthogonal to the imaging plane are also aligned with the in-plane principal strain-rates. Therefore, conditioning the principal strain-rate measurements to exclude those instances where the local flamelet-normal vector has a significant through-plane component has the effect of also limiting the data to those instances where the in-plane principal strain-rate is representative of the 3D principal strain-rate tensor. This was accomplished in the present study using crossed-plane OH-PLIF to measure the 3D flamelet-normal vector.

3.2 Flame front detection

It is well-established that the OH-combustion radical persists in post-combustion gases of lean methane-air flames over a time-scale significantly longer than that of the heat-releasing reactions and that it is therefore not a direct marker of the flame location. Nonetheless, OH-PLIF images from flames in the thin flame regime are very well suited to extract the flame front location by identifying the high gradient in the OH fluorescence signal between the unburnt and burnt gases [21]. The processing steps used in this work are as follows.

First, a background image was acquired in the absence of the flame and subtracted from all raw images. A white field correction was performed to account for inhomogeneities in the imaging system sensitivity, based on the ensemble average of 2000 images of a uniformly illuminated white target. Non-uniformity in the OH-PLIF illumination sheet was normalized based on the ensemble average of 1000 PLIF images of an acetone filled vapour cell placed at the burner exit. The corrected images were then smoothed with a Gaussian convolution filter (1.6mm kernel size). A nonlinear diffusion filter (Malm *et al.* [22]; contrast parameter 0.05, kernel 4 pixels, 25 iterations) was then applied to reduce noise and enhance flame contours. The flame contour was detected along the maximum gradient of OH by a Canny edge-detection algorithm [23]. The resulting binary images were thinned to single-pixel contours using a morphological thinning algorithm [24]. Finally, the resulting contours were parameterized ($x(s)$, $y(s)$ and $z(s)$), as a function of the path length parameter

(curvilinear coordinate *s*). All subsequent flame-contour quantities such as the vectors normal or tangent to the contours were calculated from the parametrically defined contour. Figure 4 shows an example of an OH-PLIF image acquired in this study. The extracted flame front contour is represented by the white line. The flamelet-normal vectors, which were oriented towards the unburnt region, are shown as white arrows.

3.3 3D flamelet-normal

Having identified reaction-zone contours as described above, the 3D flamelet-normal was determined at the line-of-intersection of the two (crossed) OH-PLIF imaging planes by projecting the tangential component of the flamelet-normal vector from the second (tilted) imaging plane into the frame of reference of the first and taking the cross-product of the two.

Figure 5 shows the probability density function (PDF) of the angle ζ between the local 3D flamelet-normal vector and the SPIV imaging plane (*i.e.* the out-of-plane angle of the local 3D flamelet-normal vector). As expected (given the quasi-2D burner configuration), the PDF peaks at $\zeta = 0°$ and has a relatively narrow distribution. The flame-strain alignment statistics (presented in detail in section 4.2) were conditioned according to ζ, with thresholds ranging from $\zeta = 36°$ down to $12°$. The same trends were seen at each threshold, albeit with increasing noise as more data points were conditioned out of the initial data set. The final threshold was set to $\zeta = 36°$, which left approximately 53000 measurements or 83% of the data after conditioning.

4 Results and discussions

4.1 Typical results

Figure 6(a) shows a typical strain-rate field measured in this study. The local flame front position (identified using the PLIF image) is represented by the white line. The background color shows the most extensive principal strain-rate, γ_1. The direction of the most-extensive principal strain-rate is

indicated by the black arrows. The mean flow of the unburnt gases in this plot is from bottom to top, with combustion products to the left of the flame-contour and reactants to the right. Note that the most extensive principal strain-rate is highest in the immediate vicinity of the flame front, where heat-release induces dilatation of the flow-field and therefore high extensive strain-rates. Figure 6(b) shows a section of the same field, magnified to better show the flow-flame interaction, with the local flamelet-normal direction illustrated with white arrows.

Figure 6(b) illustrates several characteristic features of the turbulence-chemistry interaction of this flame. Inspection of the strain-rate orientations well away from the reaction zone, *e.g.* along the columns $x = 9$-11mm, shows no preferred orientation of the most extensive principal strain-rate with respect to the nearest flamelet-normal. This is consistent with the isotropic nature of this turbulent flow. Closer to the reaction zone, for example along the column $x = 7$mm, a clear preferential alignment in the direction perpendicular to the local flamelet-normal (the white arrows) can be seen. Inspection of the strain-rate vectors in the immediate vicinity of the reaction zone however, reveals a clear majority of vectors aligned parallel to the local flamelet-normal. The re-orientation of the most extensive principal strain-rate with respect to the local flamelet-normal is indicative for a dynamic turbulence-flame interaction. In the next section the observed phenomena is investigated in a more significant, statistical way using all 24000 images.

4.2 Statistics of turbulence-flame alignment

In Fig. 6(b), probability density functions of the angle θ_1 between the most extensive principal strain-rate and the local flamelet-normal was computed at distances ranging from 0.8mm to 3.6mm upstream from the flame, in increments of 0.4mm (*i.e.* at each discrete vector spacing). To prevent errors associated with thermophoretic velocity, data within 0.8mm of the flame was not evaluated. This stand-off distance was confirmed by estimating the local temperature upstream of the flamelet using kinetics simulations (CHEMKIN). At 0.8mm from the flame, local temperature gradients are calculated to be ≈50K/mm, or 2.5% the magnitude of those at the reaction zone. Thermophoretic

effects can therefore be assumed to be negligible at this stand-off distance from the flame. The corresponding PDFs are shown in Fig. 7. The statistics confirm the phenomena identified in Fig. 6(b). At distances beyond 2.8mm from the flamelet the PDFs are essentially flat, showing no preferential orientation of the most extensive principal strain-rate with respect to the flame. At 2.4mm from the flamelet, the PDF shows increased probability of alignment angles greater than 45°, indicating an alignment of the most extensive principal strain-rate with respect to the flame. This alignment becomes more apparent at 2.0mm and 1.6mm from the flamelet. At 1.6mm (approximately 12η), alignment angles of 90° were almost twice as likely as angles of 0°, clearly indicating a preferentially perpendicular alignment of the most extensive principal strain-rate with respect to the local flamelet-normal. As one approaches the immediate vicinity of the flame, this preferential alignment begins to change. At 1.2mm from the flame, the PDF is again almost flat and at 0.8mm (approximately 6η), a clear tendency of the most extensive principal strain-rate to align preferentially parallel to the local flamelet-normal can be seen. It is noted that the transition from preferentially perpendicular to preferentially parallel alignment occurs at approximately 6 to 12η from the reaction zone. Prior research has shown [25-27] that the smallest (physical) strain-rate structures in a turbulent flow exist at the so-called viscous length scale, λ_v, which is found to be between 6 to 10η. The current results therefore indicate that the realignment of the principal strain and the flamelet-normal occurs within approximately $1\lambda_v$ of the flame. The onset of a preferentially perpendicular alignment however occurs even further upstream. In this study a preferentially perpendicular alignment was observed as far out as 2.4mm from the flame, which is approximately $20\ \eta$ or $3\ \lambda_v$.

Other length scales such as the Taylor microscale, λ, or the flame front thickness, δ_l, may also affect the alignment characteristics. Steinberg *et al.* [10], for example, report a preferentially perpendicular alignment already 4mm upstream of the flames. The authors report a ratio of Taylor microscale and flame thickness of about one. In the present study this ratio is about six times larger, which may explain why in this study the preferentially perpendicular alignment occurs closer to the

flame. Whether the ratio of Taylor scale and flame thickness affects the alignment characteristics of the flame will be addressed in a future study using results of several flames with different flame thicknesses for a given Taylor microscale.

The realignment phenomenon observed in the statistics helps clarify the inconsistency identified in prior studies of turbulence-flames interactions [7-10]. The statistics presented in Fig. 7 are consistent with both prior studies and illustrate the strong competition between heat-release induced dilatation at the flame front and fluid-dynamic strain-rate. Steinberg *et al.* [10] base their definition of flame location on the step-change in seed-particle number density induced by dilatation at the flame-front. This definition implicitly locates the flame at the outermost periphery of the region affected by heat-release reactions, where (in both studies) the most extensive principal strain-rate is observed to align preferentially perpendicular to the local flamelet-normal. Hartung *et al.* [9] identify the reaction zone based on the peak gradient-magnitudes observed in the OH-PLIF images which (based on laminar premixed flame calculations) occur at the same location as heat-releasing reactions of the flamelet, *i.e.* well within the dilatation-affected region. At that location, dilatation is dominant, which explains the observed tendency (in both studies) for the most extensive principal strain-rate to align preferentially parallel to the local flamelet-normal. Taken together, the statistics of this study indicate that high scalar gradients observed ahead of the flamelet are produced by the local turbulent flow-field, rather than destroyed by it.

5 Conclusions

Statistics of the alignment of the principal fluid-dynamic strain-rates and the local flamelet-normal in a premixed turbulent V-flame were measured using simultaneous stereo-PIV and crossed-plane OH-PLIF. Following an Eulerian approach, a statistical analysis of the alignment characteristics was performed at increasing distances ahead of the flame front. It was observed that approximately 30 η ahead of the flame, the fluid-dynamic principal strain-rates show no preferential alignment with the local flamelet-normal. With increasing proximity to the flame, the most extensive principal strain-

rate aligns preferentially perpendicular to the local flamelet-normal. In the immediate vicinity of the flame (≤ 0.8mm) the most extensive principal strain-rate aligns preferentially parallel to the local flamelet-normal. The realignment of the principal strain-rates in the immediate vicinity of the flame is clearly the result of local flow acceleration caused by heat-release at the reaction zone. As the most extensive principal strain-rate tends to align preferentially perpendicular to the local flamelet-normal outside the region of heat-release, the data indicate that high scalar gradients observed ahead of the flamelet are produced by the local turbulent flow-field, rather than destroyed by it.

Acknowledgements

Bibliography

[1] N. Swaminathan, K.N.C. Bray, Combust. Flame, 143 (2005) 549-565.
[2] N. Swaminathan, R.W. Grout, Phys. Fluids, 18 (2006) 045102-045109.
[3] G.K. Batchelor, Proc. R. Soc. Lond. A, 213 (1952) 349-366.
[4] O.R.H. Buxton, B. Ganapathisubramani, J. Fluid Mech., 651 (2010) 483-502.
[5] R.M. Kerr, J. Fluid Mech., 153 (1985) 31-58.
[6] A.Y. Klimenko, R.W. Bilger, Prog. Energy Combust. Sci., 25 (1999) 595-687.
[7] N. Chakraborty, N. Swaminathan, Phys. Fluids, 19 (2007) 045104-045111.
[8] N. Chakraborty, N. Swaminathan, Phys. Fluids, 19 (2007) 045103-045110.
[9] G. Hartung, J. Hult, C.F. Kaminski, J.W. Rogerson, N. Swaminathan, Phys. Fluids, 20 (2008).
[10] A.M. Steinberg, J.F. Driscoll, N. Swaminathan, Combust. Flame, 159 (2012) 2576-2588.
[11] D. Hurst, J.C. Vassilicos, Phys. Fluids, 19 (2007).
[12] S.B. Pope, Turbulent Flows, Cambridge University Press, Cambridge, 2000.
[13] J.F. Driscoll, Prog. Energy Combust., 34 (2008) 91-134.
[14] N. Peters, Turbulent Combustion, Cambridge University Press, Cambridge, 2004.
[15] I. Boxx, M. Stöhr, C. Carter, W. Meier, Combust. Flame, 157 (2010) 1510-1525.
[16] A.M. Steinberg, I. Boxx, C.M. Arndt, J.H. Frank, W. Meier, Proc. Combust. Inst., 33 (2011) 1663-1672.
[17] S. Pfadler, F. Dinkelacker, F. Beyrau, A. Leipertz, Combust. Flame, 156 (2009) 1552-1564.
[18] S. Pfadler, J. Kerl, F. Beyrau, A. Leipertz, A. Sadiki, J. Scheuerlein, F. Dinkelacker, Proc. Combust. Inst., 32 (2009) 1723-1730.
[19] P.S. Kothnur, N.T. Clemens, Phys. Fluids, 17 (2005) 125104-125114.
[20] J.E. Rehm, N.T. Clemens, Proc. Combust. Inst., 27 (1998) 1113-1120.
[21] R. Sadanandan, M. Stöhr, W. Meier, Appl. Phys. B, 90 (2008) 609-618.
[22] H. Malm, G. Sparr, J. Hult, C.F. Kaminski, J. Opt. Soc. Am. A, 17 (2000) 2148-2156.
[23] J. Canny, IEEE Trans. Pattern Anal. Mach. Intell., 8 (1986).
[24] L. Lam, S.-W. Lee, C.Y. Suen, IEEE Trans. Pattern Anal. Mach. Intell., 14 (1992) 869-885.
[25] K.A. Buch, W.J.A. Dahm, J. Fluid Mech., 364 (1998) 1-29.

[26] B. Ganapathisubramani, K. Lakshminarasimhan, N.T. Clemens, J. Fluid Mech., 598 (2008) 141-175.

[27] J.A. Mullin, W.J.A. Dahm, Phys. Fluids, 18 (2006) 035102-035128.

[28] N. Soulopoulos, J. Kerl, T. Sponfeldner, F. Beyrau, Y. Hardalupas, A.M.K.P. Taylor, J.C. Vassilicos, Fluid Dynamics Research, 45 (2013) 061404.
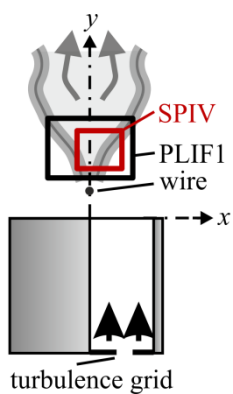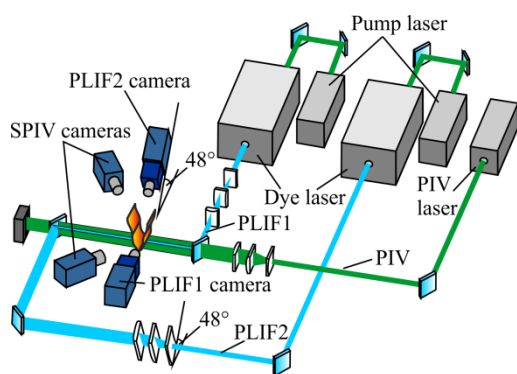
Figures and Tables

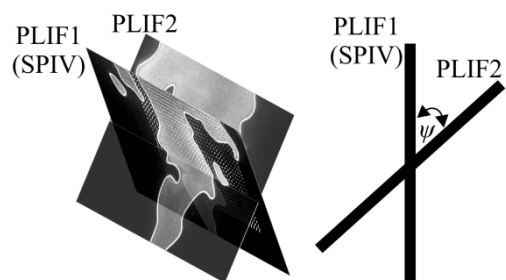Fig. 1. Schematic of the burner.

Fig. 2 Schematic of the optical setup.
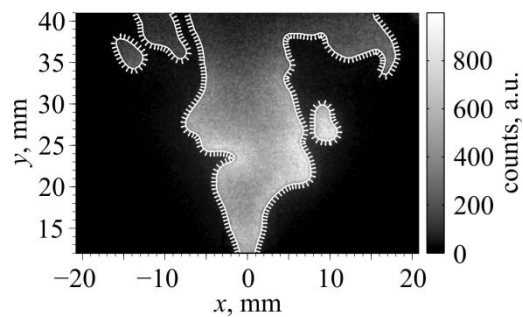

Fig. 3 Crossed-plane OH-PLIF configuration.

Fig. 4. OH-PLIF image of the premixed turbulent V-flame with the identified reaction zone overlaid in white. Local flamelet-normal vectors are shown as arrows in the direction of propagation.
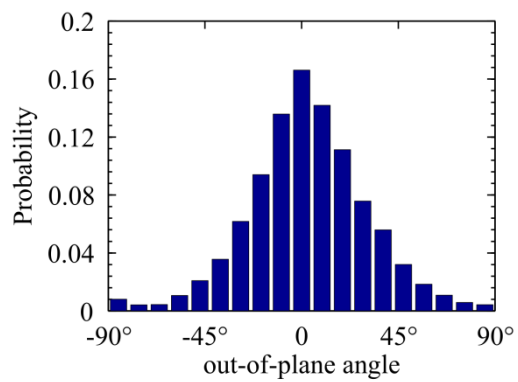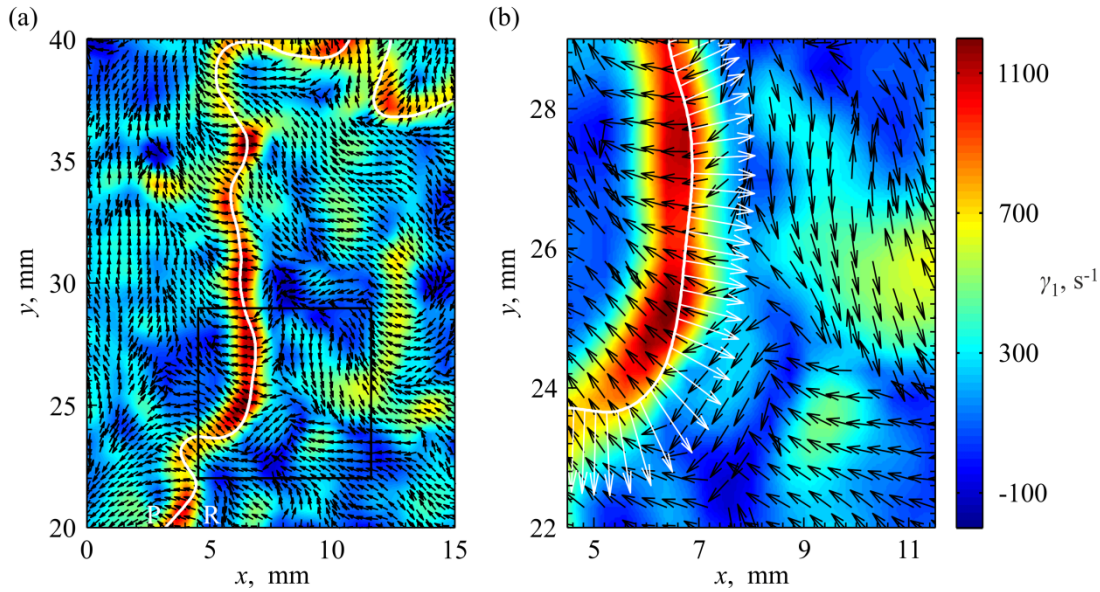

Fig. 5 Out-of-plane angle, ζ, of the flame.

Fig. 6 (a) Direction of the most extensive principal strain-rate (black arrows) superimposed upon the most extensive principal strain-rate, γ_1, in false colours. Flame front contour is represented by the white line. (b) Close-up with local flamelet-normal vectors shown as white arrows. The length of the normal vectors is 1.2mm.
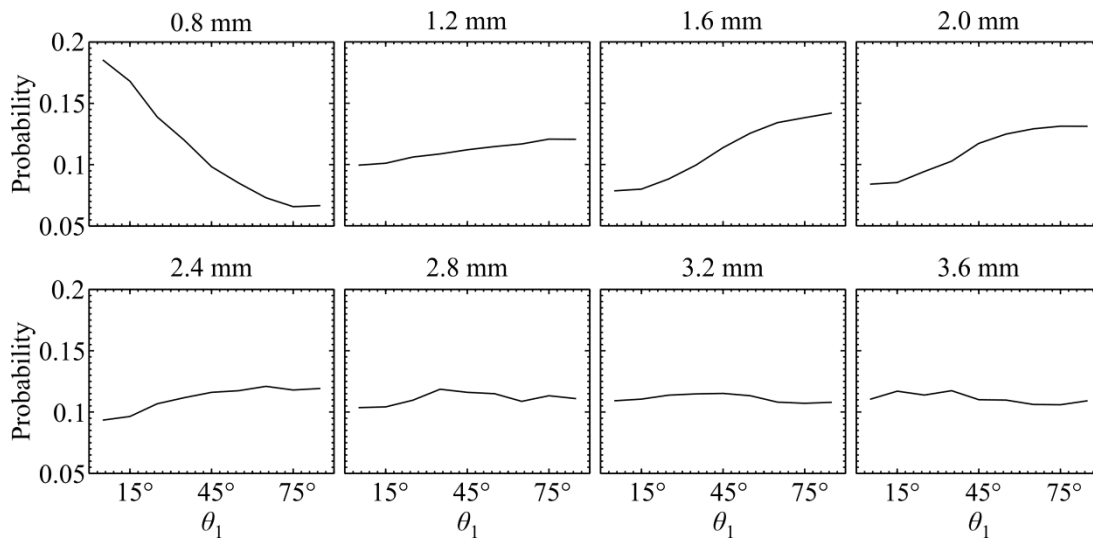

Fig. 7 PDFs of angle θ_1 between the most extensive principle strain-rate and the local flamelet-normal for various distances upstream from the flamelet.

Table 1

Isothermal turbulence properties at the wire position and flame parameters.

Property	Value	Property	Value
$\bar{u}$ (m/s)	5.5	u' (m/s)	0.75
L (mm)	9	Re_t	450
λ (mm)	3.6	η (mm)	0.12
s_l (m/s)	0.25	δ_l (mm)	0.55
Da	5.5	Ka	0.8